# Structural, Optical, and Catalytic Support Properties of γ-Al2O3 Inverse Opals

**6 AUTHORS**, INCLUDING:

Geoffrey I.N. Waterhouse
University of Auckland
105 PUBLICATIONS   1,604 CITATIONS

SEE PROFILE

Wan-Ting Chen
University of Auckland
13 PUBLICATIONS   79 CITATIONS

SEE PROFILE

Andrew Chan
University of Auckland
11 PUBLICATIONS   15 CITATIONS

SEE PROFILE

# Structural, Optical, and Catalytic Support Properties of γ-Al₂O₃ Inverse Opals

Geoffrey I. N. Waterhouse,*[,†,‡,§] Wan-Ting Chen,[†] Andrew Chan,[†] Haishun Jin,[∥] Dongxiao Sun-Waterhouse,[†] and Bruce C. C. Cowie[⊥]

[†]School of Chemical Sciences, The University of Auckland, Auckland 1142, New Zealand

[‡]The MacDiarmid Institute for Advanced Materials and Nanotechnology, Wellington 6140, New Zealand

[§]The Dodd-Walls Centre for Photonic and Quantum Technologies, Dunedin 9016, New Zealand

[∥]SAIT China Lab, Samsung R&D Institute, Beijing 100028, China

[⊥]Australian Synchrotron, Melbourne, Vic 3168, Australia

**Ⓢ** *Supporting Information*

**ABSTRACT:** Colloidal crystal templating is a versatile and inexpensive method for the fabrication of 3-dimensional photonic crystals. Here we describe the successful use of the method to fabricate γ-alumina (γ-Al₂O₃) inverse opal thin films and powders, possessing pseudo photonic bandgaps (PBGs) along the [111] direction at visible wavelengths. The optical properties of γ-Al₂O₃ inverse opal films were investigated in detail for the first time and closely obeyed a modified Bragg's law expression. The PBGs red-shifted on immersion in organic solvents, with the magnitude of the shift being directly proportional to the solvent refractive index. Calcination of the γ-Al₂O₃ inverse opals (BET area 250−275 m² g⁻¹) at temperatures from 550 to 1200 °C resulted in the stepwise transformation γ-Al₂O₃ → δ-Al₂O₃ → θ-Al₂O₃ → α-Al₂O₃. The onset temperatures for the latter polymorphic transitions were ca. 50−100 °C higher for Al₂O₃ inverse opals compared to a sol−gel alumina nanopowder, suggesting that the inverse opal architecture imparts sintering resistance. Au/γ-Al₂O₃ catalysts synthesized using γ-Al₂O₃ inverse opal supports demonstrated excellent activity for CO oxidation, with 69% CO conversion being achieved at 20 °C and near-complete conversion at 150 °C. The hierarchical porosity and high specific surface areas of γ-Al₂O₃ inverse opal powders make them near ideal supports for catalytic applications that traditionally utilize γ-alumina.
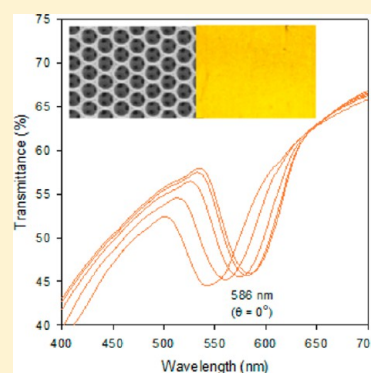
## 1. INTRODUCTION

The field of photonic bandgap engineering has evolved rapidly over the past two decades, spurred on by the development of new and improved techniques for 3-dimensional photonic crystal fabrication, including nanolithography, reactive ion etching, laser micromachining, and colloidal crystal templating. These techniques are generally classified as top-down or bottom-up, depending on the initial form of the dielectric material from which the photonic crystal is fabricated. Top-down techniques typically have their origin in the semi-conductor industry and are frequently used to impart periodic structure at micron-length scales into high dielectric materials such as Si or Ge as well as metals and polymers.[1−11] The resulting 3-dimensional photonic crystals operate at near-infrared (NIR) wavelengths and target applications such as waveguides and optical switches in communication systems. However, top-down techniques by their very nature are expensive and slow and generally only capable of fabricating photonic crystals with a maximum of 5−15 structural layers periodicity. In contrast, bottom-up methods involving colloidal crystal (opal) fabrication and colloidal crystal templating readily allow the fabrication of 3-D photonic crystals with submicron periodicity and 5−1000 structural layers periodicity.[11−38] The

colloidal crystal template method has been used to fabricate inverse opal photonic crystals in an extraordinarily diverse range of materials, including metals,[16−20] metal oxides,[21−32] carbons,[33,34] conducting polymers,[35,36] biopolymers,[37] gels,[38] and numerous other dielectrics, with PBGs ranging from the UV to the NIR. References 11−40 merely provide a quick snapshot of the plethora of inverse opal materials which have been reported to date. Inverse opal photonic crystals fabricated by bottom-up methods generally contain more intrinsic defects than comparable architectures fabricated via top-down methods, yet still possess adequate optical and excellent physical properties that can be exploited in optical sensing and light harvesting devices, sorption, photocatalysis, and catalysis. Optimization of fabrication conditions to produce inverse opal thin films with low defect densities for optical "on chip" sensors is a strong research focus in this field.[39,40]

To realize improvements in the quality of photonic crystals fabricated by the colloidal crystal template route, the four key steps in the process must be carefully controlled and optimized.

These steps comprise (1) synthesis of monodisperse, submicron sized spherical colloids, (2) crystallization of the spherical colloids on a face-centered cubic (fcc) lattice to form the colloidal crystal (opal) template, (3) infiltration of the colloidal crystal with the dielectric material of interest, and (4) selective removal of the colloidal crystal template to yield the inverse opal (the inverted replica of the template). Each of these steps has the potential to introduce disorder which will impact the optical properties of the final inverse opal product. Step 1 is the easiest to satisfy, since batches of monodisperse silica colloids of diameter 100−900 nm can readily be synthesized by the Stöber method[39−41] and monodisperse polystyrene (PS) or poly(methyl methacrylate) (PMMA) colloids with diameters 150−500 nm readily obtained by surfactant-free emulsion polymerization of styrene and methyl methacrylate, respectively.[20,21,42−46] Colloidal crystals are subsequently constructed from suspensions of these monodisperse colloids in ethanol or water (step 2), using gravitational sedimentation, centrifugation, microfluidics, and electrophoresis or flow controlled vertical deposition (FCVD). The latter method is especially useful for coating colloidal crystal thin films on planar substrates. Careful drying of the colloidal crystals is essential to minimize cracking. Steps 3 and 4 are arguably the most challenging in the process. Filling the interstitial voids in the colloidal crystal template with a second dielectric material can be achieved using a wide range of methods, including sol−gel, metal salt solution immersion, atomic layer deposition (ALD), chemical vapor deposition (CVD), or electrodeposition among others. The choice of method is largely dictated by the material being introduced, with the sol−gel, metal oxalate, and ALD routes favored for metal oxides like $SiO_2$, $ZrO_2$, $TiO_2$, and $Al_2O_3$, electrodeposition for Ag, Au, Si, ZnO, and polypyrrole, and CVD for Si and Ge.[12−38] Following infiltration, the colloidal crystal template is carefully removed by HF or alkali etching for $SiO_2$ colloids, and solvent etching or calcination for PS or PMMA templates. Successful completion of steps 1−4 yields 3-dimensionally ordered macroporous inverse opals (IOs) with a solid volume fraction ($\phi_{solid}$) between 5 and 26% depending on the extent to which the original colloidal crystal template ($\phi_{solid}$ = 74%) was infiltrated. The periodically modulated refractive index that exists in both the colloidal crystal templates and their inverse opal photonic replicas create photonic band gaps (stop bands) along particular directions in their fcc lattices,[12−48] with the width of the PBGs dependent on the solid volume fraction and dielectric contrast in the inverse opal and the defect density.[49−52] A key feature of the colloidal crystal template technique is hierarchical porosity that is achievable with many materials, particularly those which are intrinsically micro- or mesoporous such as carbons or metal oxides. However, the potential utilization of inverse opals in optical sensing applications requires improved methods for the fabrication of robust and high optical quality thin films.

γ-Alumina (γ-$Al_2O_3$) is widely used as a catalyst and a catalyst support in the automotive and petroleum industries[53−63] due to its low cost, desirable textural properties such as high surface area and mesoporosity, and also its thermal stability. Co/γ-$Al_2O_3$ catalysts demonstrate excellent activity and stability for the Fischer−Tropsch (FT) reaction,[53] while Ni/γ-$Al_2O_3$ catalysts find application in steam reforming of ethanol and methane.[53,54] Au/γ-$Al_2O_3$ catalysts are active for the oxidation of CO at room temperature.[57−60] Recently, Shimizu et al. reported that subnanometer sized silver clusters supported by

γ-$Al_2O_3$ catalyzed the C−C cross-coupling of secondary and primary alcohols. Structure−activity relationship studies determined that the reaction proceeds by a cooperation of coordinatively unsaturated silver sites and acid−base sites on the γ-$Al_2O_3$ support.[61] The high surface area and large open macropores of inverse opals potentially offer great advantages for catalytic applications involving γ-$Al_2O_3$, as several recent studies have demonstrated.[62,63] Gaun et al. found that Pd-loaded γ-$Al_2O_3$ inverse opal catalysts demonstrated better activity for catalytic methane combustion compared to catalysts prepared using dense γ-$Al_2O_3$ supports.[62] The same group also found that Pt−Rh/γ-$Al_2O_3$ inverse opal catalysts showed high efficiency for CO oxidation.[63] Further studies are necessary to gauge the full potential of γ-$Al_2O_3$ inverse opals as a catalytic support. In addition, the optical properties of inverse opal γ-$Al_2O_3$ thin films and powders and also their thermal behavior have not yet been well documented, motivating a detailed investigation.

This study aimed to fill a number of the critical knowledge gaps identified above concerning the physical, optical, and catalytic properties of γ-$Al_2O_3$ inverse opals. Specific objectives were (1) the fabrication of a series of γ-$Al_2O_3$ inverse opal thin films and powders with PBGs at visible wavelengths, (2) full optical characterization of the γ-$Al_2O_3$ inverse opal thin films, (3) investigation of the thermal stability and polymorphic transformations of γ-$Al_2O_3$ inverse opals, and (4) synthesis of a 5 wt % Au/γ-$Al_2O_3$ inverse opal catalyst and investigation of its performance for low-temperature CO oxidation. It was envisaged that collectively this information would serve as a useful platform for other researchers seeking to exploit γ-$Al_2O_3$ inverse opals in different applications.

## 2. EXPERIMENTAL SECTION

**2.1. Materials.** Methyl methacrylate (MMA, 99%), 2,2′-azobis(2-methylpropionamidine) dihydrochloride (97%), aluminum tri-*sec*-butoxide (97%), 2-butanol (99%), concentrated HCl (37 wt % in water), tetrachloroauric acid trihydrate (≥99.8%), and urea (99%) were all obtained from Sigma-Aldrich and used without further purification. A γ-$Al_2O_3$ sol−gel nanopowder was prepared from aluminum tri-*sec*-butoxide using a literature procedure.[64]

**2.2. Synthesis of Monodisperse Poly(methyl methacrylate) Colloids.** Three different batches of monodisperse PMMA colloids (denoted as PMMA #1−3) were synthesized by the surfactant-free emulsion polymerization of methyl methacrylate in water at 70−80 °C.[22] Briefly, methyl methacrylate (0.3 L for PMMA #1 and PMMA #2, 0.4 L for PMMA #3) and water (1.6 L) were added to a 5-necked round-bottom flask (3 L volume), fitted with a mechanical stirrer (Teflon shaft and stirrer blade), thermometer, water-cooled reflux condenser, nitrogen tube, and a glass stopper. The contents of the flask were then heated under $N_2$ and vigorous mechanical stirring to 70 °C (for PMMA #2 and PMMA#3) or 80 °C (for PMMA #1), whereupon the initiator 2′-azobis(2-methylpropionamidine) dihydrochloride (1.5 g) was quickly added. The reaction was then allowed to proceed for 3 h at the specified temperature, after which the resulting PMMA colloid suspensions were allowed to cool slowly to room temperature over a period of 1−2 h under a nitrogen purge. The colloid suspensions were subsequently filtered through glass wool to remove any large agglomerates and stored in PET bottles. Colloid diameters determined by DLS and TEM for PMMA

#1, PMMA #2, and PMMA #3 were 313, 352, and 394 nm, respectively.

**2.3. Fabrication of PMMA Colloidal Crystals.** Three-dimensional PMMA colloidal crystals were constructed from the PMMA colloid suspensions by two methods: centrifugation and flow-controlled vertical deposition (FCVD).[22] In the centrifugation method, undiluted PMMA colloid suspension (50 mL) was poured into a 50 mL polypropylene Falcon tube, capped, and centrifuged at 1500 rpm (rcf 369) for 24 h. The supernatant was then carefully removed with a Pasteur pipet, and the resulting colloidal crystals left to dry in air at 25 °C for 2−3 weeks. The FCVD method was used to deposit thin PMMA colloidal thin films on glass microscope slides for UV−vis transmittance measurements. Briefly, PMMA colloid suspension (50 mL) was diluted 5−6-fold with Milli-Q water and then poured into a vertical-walled glass beaker (diameter 10 cm, height 5 cm). A number of precleaned glass microscope slides were then immersed vertically in the colloid suspension, after which a peristaltic pump was used to remove the colloidal suspension (pump rate about 0.2 mL min$^{-1}$). As the liquid was slowly pumped away, a thin colloidal crystal layer of 5−10 $\mu$m thickness deposited on the glass slides at the falling meniscus. Films were dried in air at 25 °C overnight.

**2.4. Fabrication of $\gamma$-Al$_2$O$_3$ Inverse Opal Films and Powders.** $\gamma$-Al$_2$O$_3$ inverse opal powders and films of were prepared by filling the interstitial voids in PMMA colloidal crystal templates described above with a $\gamma$-Al$_2$O$_3$ sol−gel precursor and then carefully calcining the resulting composite structure to remove the PMMA template. To make the $\gamma$-Al$_2$O$_3$ inverse opal powders, the monolithic PMMA colloidal crystals obtained by centrifugation were first lightly crushed with a metal spatula to give fractured pieces of size <2 mm and then deposited as a 5 mm thick layer on filter paper (Whatman grade 1, 185 mm diameter, prewetted with 2-butanol) in a large Büchner funnel. With a strong vacuum applied to the Büchner funnel, a solution of 50 wt % aluminum tri-*sec*-butoxide in 2-butanol was applied quickly dropwise over the surface of the PMMA colloidal crystal layer. The vacuum was applied for a further 30 min to remove excess solution, after which infiltrated samples were dried in air at 25 °C for 72 h. The composites were then transferred to porcelain evaporating basins and calcined using the following protocol to remove the PMMA templates: 25 to 300 °C at 1 °C min$^{-1}$; held at 300 °C for 3 h; then ramped from 300 to 550 °C at 2 °C min$^{-1}$; and held at 550 °C for 4 h; then slowly cooled to room temperature over 3−4 h. The resulting $\gamma$-Al$_2$O$_3$ inverse opals powders (denoted as $\gamma$-Al$_2$O$_3$ #1−3) all displayed visible opalescence under incident white light. For the fabrication of $\gamma$-Al$_2$O$_3$ inverse opal thin films, a 5 wt % aluminum tri-*sec*-butoxide in 2-butanol solution was applied dropwise along one edge of the PMMA colloidal crystal films (on glass substrates). A combination of capillary action and gravity resulted in the successful infiltration of the colloidal crystal templates with the sol−gel solution. $\gamma$-Al$_2$O$_3$ inverse opal thin films were subsequently obtained by applying the calcination protocol described above for the powders.

**2.5. Synthesis of 5 wt % Au/$\gamma$-Al$_2$O$_3$ Catalysts.** Au nanoparticles were deposited on both the $\gamma$-Al$_2$O$_3$ inverse opal and the reference sol−gel derived $\gamma$-Al$_2$O$_3$ nanopowder using the deposition−precipitation with urea method. Briefly, $\gamma$-Al$_2$O$_3$ (1 g) was added with gentle stirring to a 100 mL aqueous solution of HAuCl$_4$·3H$_2$O (0.1052 g) and urea (3 g) in a 250 mL glass Schott bottle. The suspension containing $\gamma$-Al$_2$O$_3$ was then heated with gentle stirring to 80 °C and maintained at this temperature for 8 h. The obtained yellow Au(III) impregnated $\gamma$-Al$_2$O$_3$ powders were collected by vacuum filtration, washed with Milli-Q, and air-dried at 70 °C for 2 h. Calcination at 300 °C for 2 h reduced surface Au(III) to Au$^0$, yielding red-purple Au/$\gamma$-Al$_2$O$_3$ powders.

**2.6. Characterization.** SEM images were collected using a Philips XL-30 field emission gun scanning electron microscope (FEGSEM). All micrographs were collected at an electron gun accelerating voltage of 5 kV. Specimens were mounted on black carbon tape and platinum sputter-coated for analysis.

TEM images were taken on a TECNAI 12 transmission electron microscope. Samples were dispersed in absolute ethanol, and then 3 $\mu$L of the resulting dispersion was placed on carbon-coated copper TEM grids for analysis.

Powder XRD patterns were acquired on a Siemens D5000 diffractometer equipped with a Cu anode X-ray tube and a curved graphite filter monochromator. XRD data were collected from $2\theta = 10°−90°$ (step 0.02°, scan rate 2° min$^{-1}$) using Cu K$\alpha$ X-rays ($\lambda = 1.5418$ Å, 40 mA, 40 kV). Al$_2$O$_3$ phases were identified by reference to standard spectra in the JCPDS database.

UV−vis transmittance spectra were recorded over the range 200−1000 nm on a Shimadzu UV-1700 PharmaSpec UV−vis spectrophotometer, equipped with a custom-built sample holder for angle-resolved UV−vis transmittance measurements.

Photonic bandgap simulations for the Al$_2$O$_3$ inverse opals in air were based on a plane-wave expansion method, using the MPB software package developed at MIT.[65] A refractive index of 1.6 was assumed for Al$_2$O$_3$.[66] The lattice constant ($a$) in the simulated band structure was determined as the center-to-center distance between spheres ($D$) multiplied by the square root of 2.

XPS data were collected using a Kratos Axis UltraDLD equipped with a hemispherical electron energy analyzer and an analysis chamber of base pressure ~1 × 10$^{-9}$ Torr. Spectra were excited using monochromatic Al K$\alpha$ X-rays (1486.69 eV), with the X-ray source operating at 150 W. The spectra were calibrated against the C 1s signal at 285.0 eV from adventitious hydrocarbons.

Al K-edge NEXAFS data were collected on the soft X-ray Beamline at the Australian Synchrotron. NEXAFS data were taken in the partial electron yield (PEY) mode at an analysis chamber pressure of ~1 × 10$^{-10}$ Torr. The PEY data were normalized against a current measured simultaneously on a gold mesh in the beamline to eliminate potential spectral artifacts caused by fluctuations in the beam intensity while scanning. The measurements were carried out in high resolution (HR) mode by increasing the photon energies in steps of 0.05 or 0.1 eV.

TGA analyses were performed on a Shimadzu TGA-50 thermogravimetric analyzer. Selected photocatalysts were heated in air from room temperature to 1000 °C at a heating rate of 5 °C min$^{-1}$.

N$_2$ physisorption isotherms were determined at liquid nitrogen temperature (−195 °C) using a Micromeritics Tristar 3000 instrument. Specific surface areas were calculated from the N$_2$ adsorption data according to the Brunauer−Emmett−Teller (BET) method using $P/P_0$ values in the range 0.05−0.2. Cumulative pore volumes and pore diameters were calculated from the adsorption isotherms by the Barrett−Joyner−Halenda (BJH) method. Samples were degassed at 150 °C under vacuum for 2 h prior to the N$_2$ physisorption measurements.
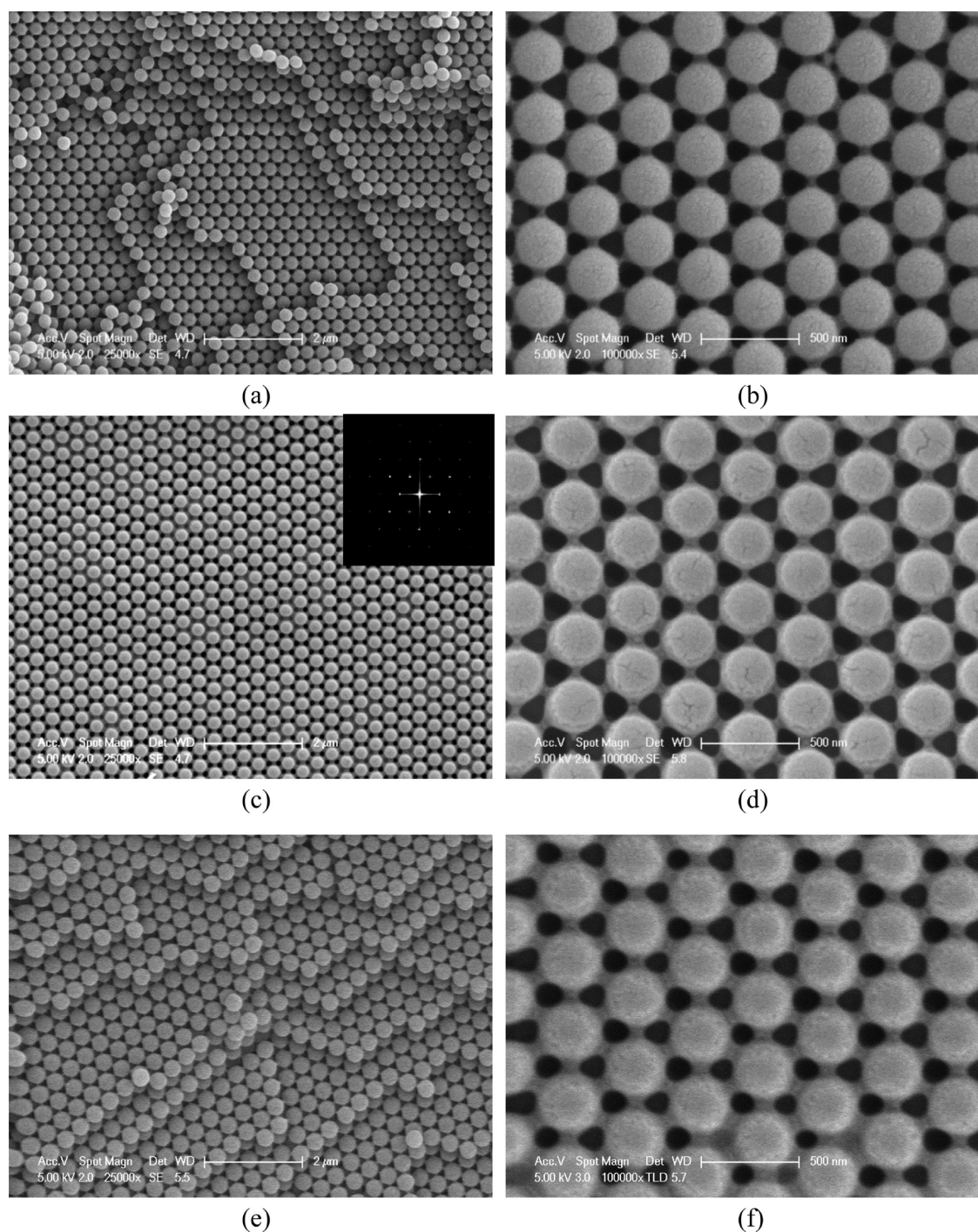
**Figure 1.** SEM micrographs for PMMA colloidal crystal films used as sacrificial templates in the fabrication of γ-Al$_2$O$_3$ inverse opal films. (a, b) PMMA #1; (c, d) PMMA #2; and (e, f) PMMA #3. Images on the left were taken at 25 000× magnification and those on the right at 100 000× magnification. The inset in Figure 1c shows the Fourier transform of the corresponding image and highlights the long-range order achieved in the PMMA colloidal crystal templates.

**2.7. Catalytic Activity Tests.** The activity of the Au/γ-Al$_2$O$_3$ catalysts for CO oxidation at temperatures between 25 and 200 °C was evaluated in a fixed bed glass reactor (i.d. 6 mm) containing 0.25 g of catalyst supported on a porous glass frit. No catalyst activation procedure was used. Experiments were conducted by passing a reactant gas mixture containing CO and O$_2$ (4 vol % in He, CO/O$_2$ = 2/1, total flow rate 50 mL min$^{-1}$) through the catalyst bed. The reactants and products were analyzed using a Shimadzu GC-2014 gas chromatograph equipped with a 5 Å molecular sieve column and a thermal conductivity detector.

## 3. RESULTS

**3.1. PMMA Colloidal Crystal Template Characterization.** PMMA colloidal crystals prepared by centrifugation and the FCVD method were near identical in all aspects, so the discussion below concentrates primarily on the physical and optical properties of the PMMA colloidal crystal films. Figure 1

**Table 1. Summarized Physical and Optical Data for the PMMA Colloidal Crystals and Their Inverse Opal $Al_2O_3$ Replicas[a]**

| sample | BET surface area (m² g⁻¹) | optical data and derived constants | | | | | | |
|---|---|---|---|---|---|---|---|---|
| | | $D_{SEM}$ (nm) | $D_{UV-vis}$ (nm) | $n_{avg}$ | $\phi$ | $\lambda_{max}$ (nm) $\theta = 0°$ | $\Delta\lambda/\lambda_{max}$ | $a/\lambda_{max}$ |
| PMMA #1 | | 313 | 315 | 1.357 | 0.726 | 698 | 0.073 | 0.634 |
| PMMA #2 | | 352 | 353 | 1.363 | 0.738 | 786 | 0.074 | 0.633 |
| PMMA #3 | | 394 | 397 | 1.352 | 0.715 | 877 | 0.074 | 0.635 |
| $\gamma$-$Al_2O_3$ #1 | 275.5 | 264 | 264 | 1.073 | 0.122 | 463 | 0.111 | 0.806 |
| $\gamma$-$Al_2O_3$ #2 | 238.4 | 305 | 307 | 1.064 | 0.106 | 534 | 0.112 | 0.808 |
| $\gamma$-$Al_2O_3$ #3 | 245.5 | 334 | 340 | 1.054 | 0.089 | 586 | 0.109 | 0.804 |

[a]$D$ = center-to-center distance between spheres on fcc(111) planes. Differences between $D_{SEM}$ and $D_{UV-vis}$ for each sample are negligible given the ±1−2% uncertainty in the determination of $D$ by each method.

shows SEM images for thin films constructed from the three different batches of PMMA colloids using the FCVD method, viewed along the [111] direction of the crystals. The films were approximately 7 $\mu$m thick. The images on the left taken at 25 000× confirm the monodispersity of the individual batches of PMMA colloids, while the fracture surfaces (Figure 1a,e) reveal the characteristic ABC packing sequence expected for a fcc lattice. The Fourier transform conducted on a 6 × 6 $\mu$m region of Figure 1c provides additional evidence for excellent long-range order in the sample. The images on the right taken at 100 000× magnification show a progressive increase in the size of the colloids between PMMA #1, #2, and #3 (Figure 1b,d,f) and also that the individual colloids in the templates are physically connected to one another through narrow PMMA bridges. This bridging is inherently beneficial to latter colloidal crystal templating steps as it confers a degree of mechanical rigidity to the 3D structure.

Centre-to-center distances ($D$) between colloids on the fcc(111) planes determined directly from the SEM images were 313, 352, and 394 nm for PMMA #1, #2, and #3, respectively (Table 1). Because of their high structural uniformity, the colloidal crystal films showed vibrant angle-dependent structural color at visible wavelengths (for PMMA #2 and #3, the opalescence was visible at grazing incident angles with respect to the surface plane). UV−vis transmittance spectra collected from the PMMA colloidal crystal thin films at normal incidence ($\theta = 0°$) are shown in Figure S1 and confirm photonic bandgaps (transmittance minima) at 698, 786, and 877 nm. Since the PMMA colloidal crystal films crystallize with their fcc(111) plane parallel to the underlying glass substrate, these photonic bandgaps can readily be assigned to first-order Bragg diffraction on fcc(111) planes. The red-shift in the photonic bandgap position with increasing colloid diameter ($D$) is consistent with the modified Bragg's law expression (eq 1), typically used to describe the optical properties of opal and inverse opal photonic crystals.[10−38]

$$\lambda_{max} = 1.633D\sqrt{n_{avg}^2 - \sin^2\theta} \tag{1}$$

where $\lambda_{max}$ is the PBG position (in nm) for first-order diffraction on fcc(111) planes, $D$ is the center-to-center distance between colloids on the (111) planes (in nm), $n_{avg}$ is the average refractive index of the photonic structure, and $\theta$ is the incident angle of light with respect to the surface normal of the fcc(111) plane. By convention, the optical properties of photonic crystals are described in terms of their reflectance characteristics, hence the use of the term $\lambda_{max}$ (here were present transmittance spectra wherein $\lambda_{max}$ will appear as a local transmittance minimum at the same wavelength). The average refractive index is calculated using the formula $n_{avg} = \phi n_{solid} + (1$

$- \phi)n_{void}$, where $\phi$ is the solid volume fraction and $n_{solid}$ and $n_{void}$ are the refractive indices of the solid and void components. PMMA has a refractive index of 1.492, so assuming an ideal solid volume fraction of 0.74 for a fcc array of solid spheres, the theoretical $n_{avg}$ for a PMMA colloidal crystal in air is 1.364. Using this value, together with the $D$ values of 313, 352, and 394 nm determined by SEM, eq 1 predicts that PMMA #1, #2, and #3 films should display photonic band gaps at 697, 784, and 888 nm when $\theta = 0°$, in near perfect accord with the experimentally determined values of 698, 786, and 877 nm (Figure S1 and Table 1). By collecting transmittance spectra at different angles of incidence with respect to the (111) plane and plotting $\lambda_{max}^2$ versus $\sin^2\theta$, a straight line was obtained for each colloidal crystal film (not shown) with slope = $-1.633^2D^2$ and y-axis intercept = $1.633^2D^2n_{avg}^2$. Values for $D$, $n_{avg}$, and $\phi$ determined from the analyses are summarized in Table 1 and were again in excellent accord with theory. Normalized bandwidths ($\Delta\lambda/\lambda_{max}$, where $\Delta\lambda$ is the fwhm of the PBG) and normalized frequencies ($a/\lambda_{max}$, where $a = (2^{1/2}\times D)$ of the PBGs were identical for the three different PMMA colloidal crystals (Table 1), highlighting their inherent structural and compositional similarity and uniformity.

**3.2. Structural and Optical Characterization of $\gamma$-$Al_2O_3$ Inverse Opals.** The excellent structural order of the PMMA colloidal crystal templates was largely preserved in the fabrication of their $\gamma$-$Al_2O_3$ inverse opal replicas. Figure S2 shows SEM images for the same PMMA #3 thin film on glass, before and after the colloidal crystal templating procedure. The PMMA colloidal crystal film was continuous, completely covering the glass substrate (Figure S2a). In contrast, the $\gamma$-$Al_2O_3$ #3 film was discontinuous (Figure S2c), taking the form of islands of size 500−2000 $\mu$m² on the glass substrate. Clearly, the fcc structure underwent significant shrinkage during the inversion step. Using the $D$ values on the fcc(111) planes as a guide, the shrinkage was estimated to be approximately 15% in all three spatial dimensions, corresponding to a geometric volume loss (length × breadth × height) of $(0.85)^3$ or 39%. Remarkably, in spite of the shrinkage of the film, the individual $\gamma$-$Al_2O_3$ #3 islands retained excellent fcc order with their (111) planes parallel to the underlying substrate (Figure S2d). The SEM images presented in Figure 2 for $\gamma$-$Al_2O_3$ #1 and #3 thin films confirmed this. Center-to-center distances between macropores ($D$) measured directly from Figures 2b and 2d were 264 and 334 nm, respectively (cf. the $D$ values for the corresponding PMMA templates were 313 and 394 nm, respectively (Table 1), hence confirming that 15% reduction in $D$ on inversion). Figure 2e shows a $\gamma$-$Al_2O_3$ #3 powder, which also bares strong resemblance to its PMMA template (Figure 1e). The overall success of the templating procedure was evident visually (Figure 2f), with the reflected color of light
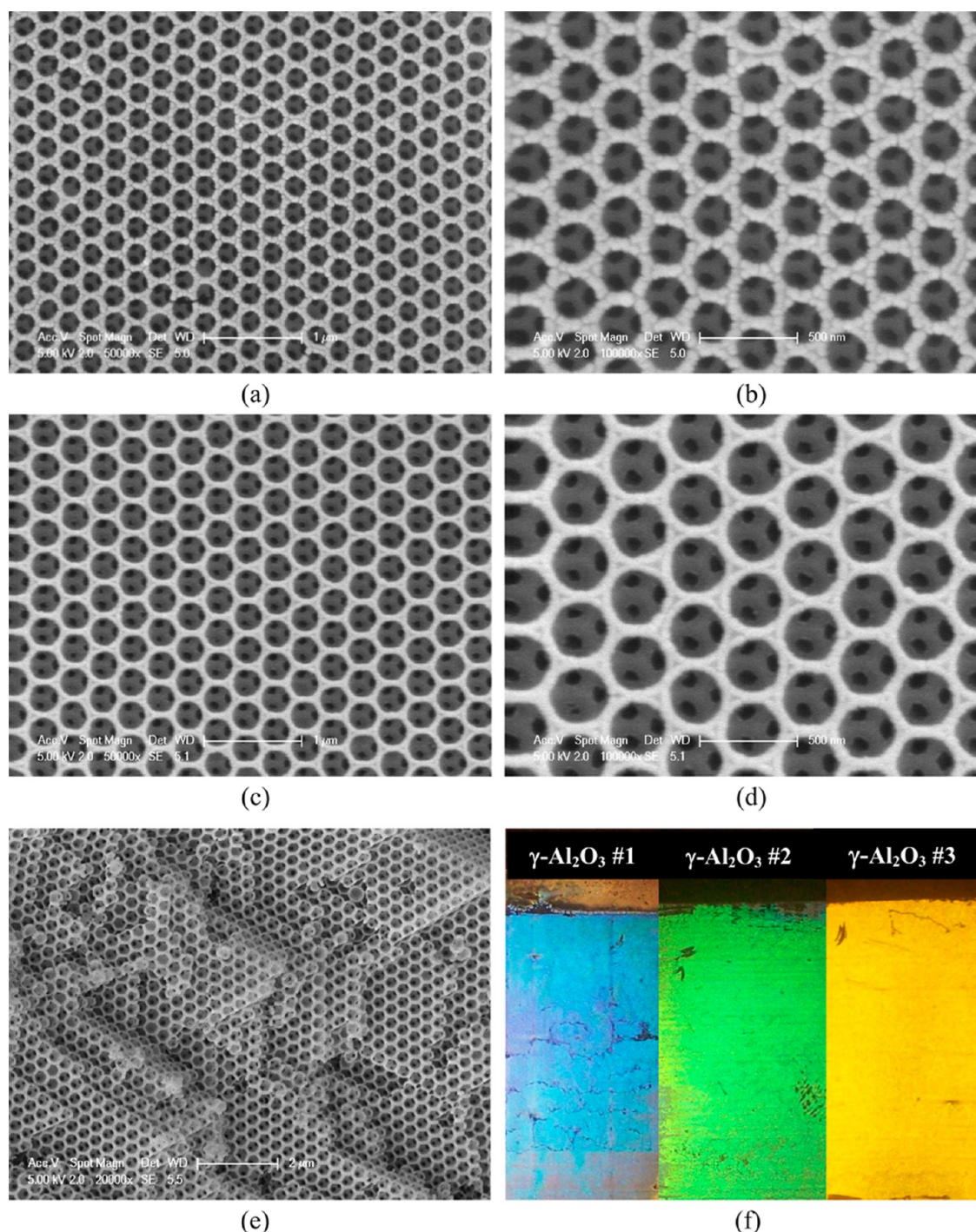
**Figure 2.** SEM micrographs for alumina inverse opals fabricated using the colloidal crystal template method. (a, b) $\gamma$-Al$_2$O$_3$ #1 thin film viewed along the [111] direction; (c, d) $\gamma$-Al$_2$O$_3$ #3 thin film viewed along the [111] direction; and (e) $\gamma$-Al$_2$O$_3$ #3 powder. (f) Digital photographs of the $\gamma$-Al$_2$O$_3$ inverse opal thin films in air, illuminated and viewed along the [111] direction.

along the [111] direction progressively red-shifting as $D$ increased (i.e., on moving left to right, $\gamma$-Al$_2$O$_3$ #1−3).

UV−vis transmittance spectra from the $\gamma$-Al$_2$O$_3$ #1−3 thin films at normal incidence ($\theta = 0°$) are shown in Figure 3a and confirm photonic band gaps along the [111] direction at 463, 534, and 586 nm, respectively. In accordance with eq 1, the PBG position showed a linear dependence on the center-to-center distance ($D$) between macropores on the fcc(111) planes (Figure 3b and Table 1). The normalized bandwidths-($\Delta\lambda/\lambda_{max}$) and the normalized frequencies ($a/\lambda_{max}$) of the

PBGs were near identical for three $\gamma$-Al$_2$O$_3$ IO samples (Table 1). Figure S3 shows a linear relationship between the PBG positions in the $\gamma$-Al$_2$O$_3$ #1−3 films and their respective PMMA templates. Such a plot is useful to researchers aiming to fabricate $\gamma$-Al$_2$O$_3$ inverse opal films with a specific PBG position by the colloidal crystal template route.

The angle dependence of the structural color in the $\gamma$-Al$_2$O$_3$ #1−3 films are examined in Figure 4. In agreement with eq 1, the PBG for diffraction on fcc(111) planes blue-shifted as the incident angle of light was increased with respect to the surface
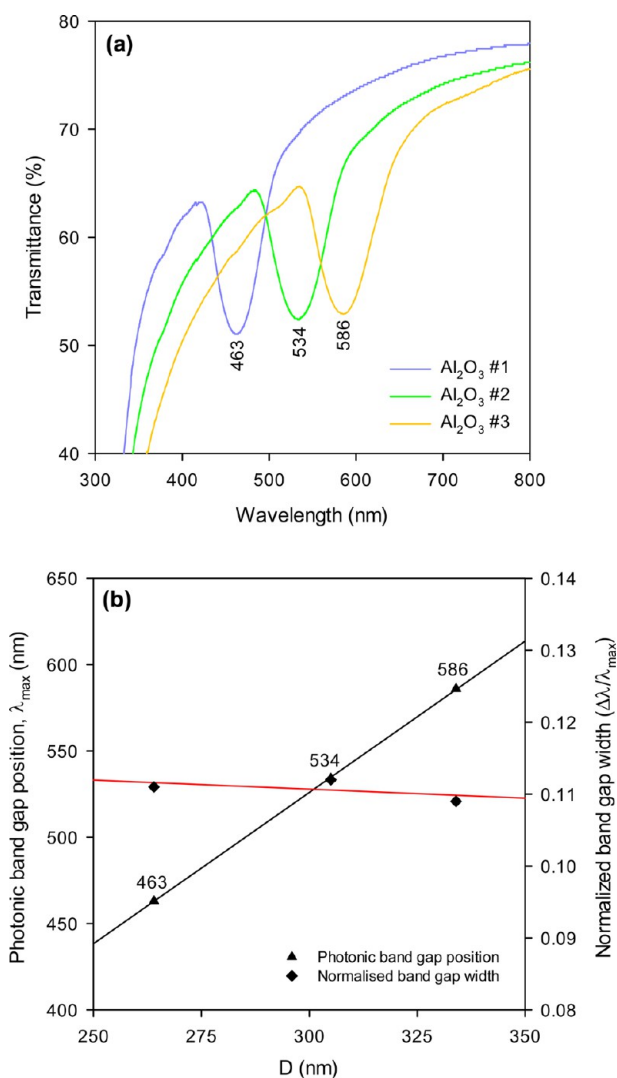
**Figure 3.** (a) UV−vis transmittance spectra for $\gamma$-$Al_2O_3$ inverse opal thin films in air showing photonic bandgaps along the [111] direction. (b) Plot of position of the photonic band gap along the [111] direction and the normalized bandgap width versus the center-to-center distance between macropores ($D$) on fcc(111) planes.

normal of the (111) plane (Figure 4a). Plots of $\lambda_{max}^2$ versus $\sin^2\theta$ for all three different $\gamma$-$Al_2O_3$ IO films yielded a straight line (Figure 4b), from which $D$, $n_{avg}$, and $\phi$ could be extracted (Table 1). $D$ values determined in the angle studies were near identical to those obtained from SEM, highlighting the close relationship between the geometric and optical properties of the photonic crystals. The average refractive index of the $\gamma$-$Al_2O_3$ IO films were in the range 1.054−1.073, corresponding to an alumina volume fraction of 8.9−12.2%, respectively (a refractive index of 1.6 was assumed in the calculating the alumina volume fraction). These values are significantly lower than the maximum theoretical value of 26% for an inverse opal, though reasonable when compared to other metal oxide inverse opals fabricated by the colloidal crystal template route.[21−32]

Figure 5 shows the photonic bandgap structure diagram obtained for a $\gamma$-$Al_2O_3$ inverse opal, constructed by assuming a solid volume fraction of 12% and an $Al_2O_3$ refractive index of 1.6. The diagram confirms the existence of a pseudo photonic bandgap between the second and third bands along the [111] direction ($L \rightarrow \Gamma$). The predicted angular frequency of the
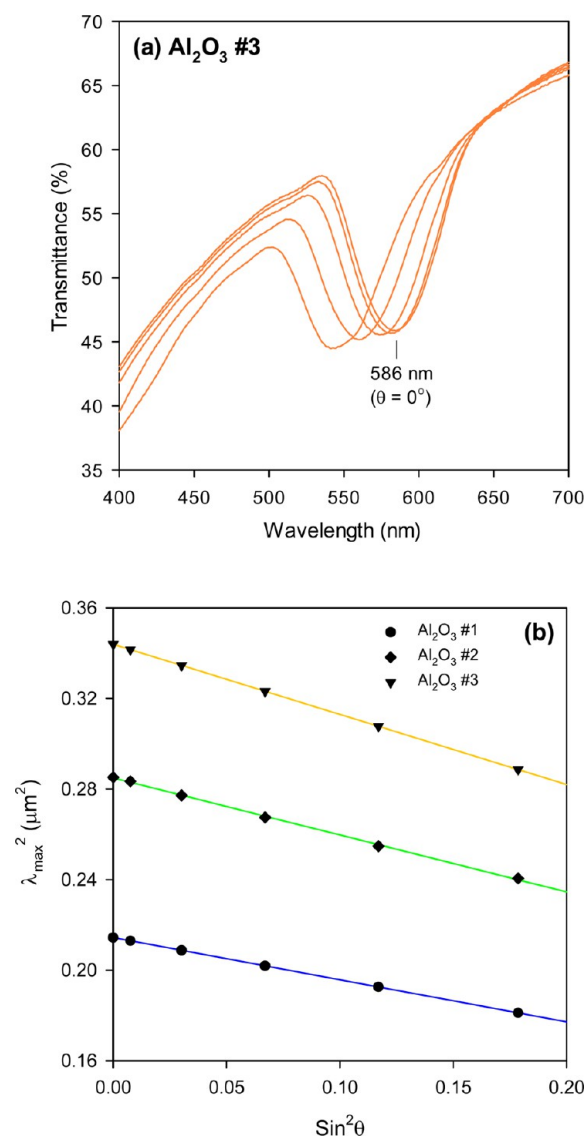
**Figure 4.** (a) UV−vis transmittance spectra collected in air for a $\gamma$-$Al_2O_3$ inverse opal film at incident angles of 0−20° with respect to the [111] direction. As the incident angle of light is increased from 0 to 20°, the photonic band gap blue-shifted in accordance with eq 1. (b) plots of $\lambda_{max}^2$ versus $\sin^2\theta$ for $\gamma$-$Al_2O_3$ #1-3 films.

PBG is 0.79, very close to the $a/\lambda_{max}$ values of 0.804−0.808 determined here experimentally for the $\gamma$-$Al_2O_3$ #1−3 films. The photonic bandgap structure diagram also predicts that the PBG will blue-shift when the films are tilted with respect to the [111] direction, in agreement with the experimental findings of Figure 4.

Optical sensing is one of the key future applications envisaged for inverse opal thin films. Figure 6a shows UV−vis transmittance spectra collected at normal incidence ($\theta = 0°$) for a $\gamma$-$Al_2O_3$ #2 film in air and a selection of organic solvents of different refractive index. The data show that as the refractive index of the medium filling the macropores in the $\gamma$-$Al_2O_3$ inverse opal film increased, the PBG for diffraction on fcc(111) planes progressively red-shifted, and the transmittance of the film at visible wavelengths increased significantly. As the refractive index contrast (RIC) between $\gamma$-$Al_2O_3$ ($n = 1.6$) and solvent filling the macropores decreased, the PBG became progressively weaker and was hardly discernible when the film

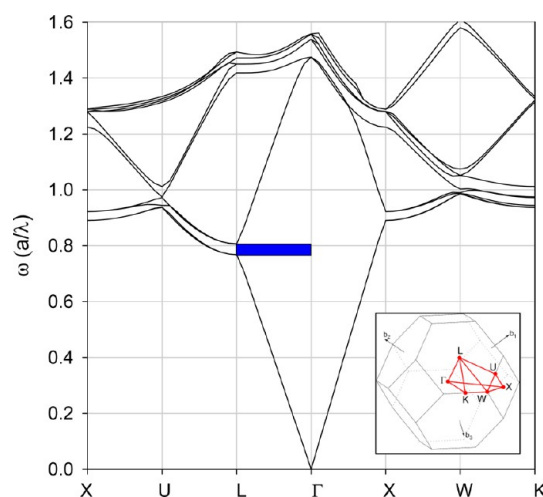**Figure 5.** Photonic band gap structure diagram for a $\gamma$-$Al_2O_3$ inverse opal showing a pseudo photonic bandgap between the second and third bands along the $L \rightarrow \Gamma$ direction (i.e., [111] direction). The inset shows the near spherical first Brillouin zone of a fcc lattice.

was immersed in bromobenzene ($n = 1.559$). The PBG is expected to completely disappear in a solvent with a refractive index of 1.6 due to the absence of any refractive index contrast (an essential requirement for any photonic crystal). Figure 6b shows the PBG position plotted as a function of solvent refractive index. Excellent linearity is obtained, in accordance with eq 2, obtained by substituting $n_{avg} = [\phi n_{solid} + (1 - \phi) n_{void}]$ into eq 1 when $\theta = 0°$ and replacing $n_{solid}$ and $n_{void}$ with $n_{Al_2O_3}$ and $n_{solvent}$, respectively

$$\lambda_{max} = 1.633 D \phi n_{Al_2O_3} + 1.633 D (1 - \phi) n_{solvent} \quad (2)$$

where $\lambda_{max}$ is the PBG position (in nm) for first-order diffraction on fcc(111) planes, $D$ is the center-to-center distance between colloids on the (111) planes (in nm), $\phi$ is the alumina solid volume fraction, $n_{Al_2O_3}$ is the refractive index of the sol–gel alumina, and $n_{solvent}$ is the refractive index of the medium filling the macropores. A plot of $\lambda_{max}$ versus $n_{solvent}$ is predicted to be linear (in agreement with experiment here), with slope = $1.633 D (1 - \phi)$ and y-axis intercept = $1.633 D \phi n_{Al_2O_3}$. By simple mathematical rearrangement, independent expressions for $D$ and $\phi$ can be obtained:[21−23]

$$D = \frac{slope \times n_{Al_2O_3} + intercept}{1.633 \times n_{Al_2O_3}} \quad (3)$$

$$\phi = \frac{intercept}{slope \times n_{Al_2O_3} + intercept} \quad (4)$$

The slope and intercept in Figure 6b were 430.4 and 102.6 nm, respectively. Substituting these values into eqs 3 and 4, and using $n_{Al_2O_3} = 1.6$, gives $D = 303$ nm and $\phi = 0.13$. These values are in remarkably good accord with those determined for $\gamma$-$Al_2O_3$ #2 by SEM and UV–vis angle studies (Table 1). Results presented in Figures 2−6 highlight the close relationship between the physical and optical properties of $\gamma$-$Al_2O_3$ inverse opals and also their potential for use in optical sensing applications.

**3.3. Thermal Transformations of $\gamma$-$Al_2O_3$ Inverse Opals and Derived Transitional Aluminas.** $\gamma$-$Al_2O_3$ is the support of choice in many catalytic applications because of its
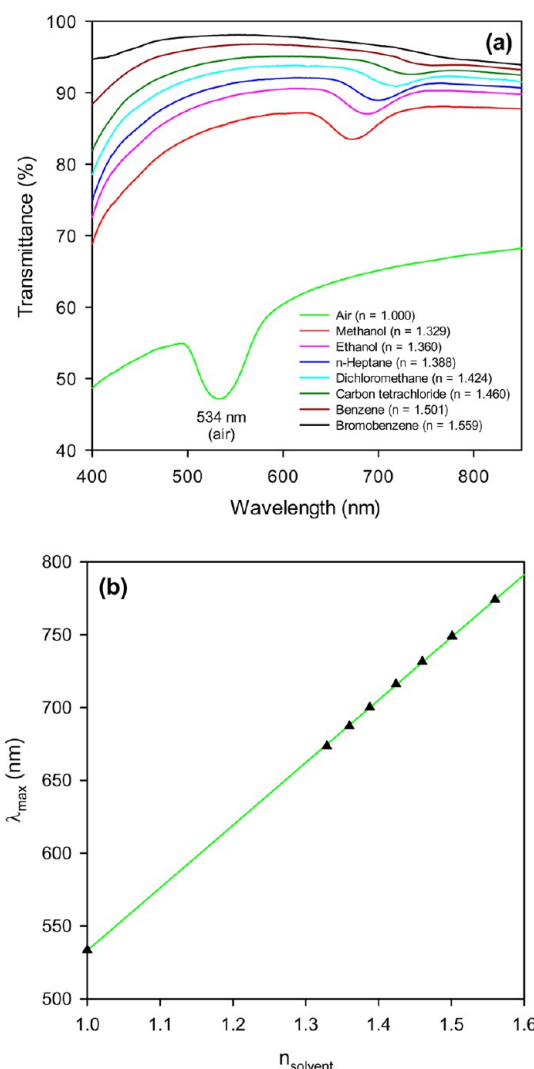




**Figure 6.** (a) UV−vis transmittance spectra collected at normal incidence ($\theta = 0°$) from a $\gamma$-$Al_2O_3$ inverse opal thin film in air ($n = 1.000$, $\lambda_{max} = 534$ nm) and then solvents of increasing refractive index. The PBG progressively red-shifted and the film became transparent as the refractive index of the solvent filling the macropores in the $Al_2O_3$ IO increased. (b) Plot of the PBG position ($\lambda_{max}$) versus $n_{solvent}$, showing a linear dependence as predicted by eq 2.

high surface area and surface acidity,[53−63] with both depending on the hydroxyl content and thermal history of a sample.[67−69] This motivated a detailed investigation of the effect of calcination temperature on the phase stability and physical and structural properties of the $\gamma$-$Al_2O_3$ inverse opals. Figure 7 shows XRD patterns for $\gamma$-$Al_2O_3$ #1 powder calcined at temperatures up to 1200 °C. The as-prepared sample was mesoporous (Figure 7a), with a BET surface area of 275.5 m$^2$ g$^{-1}$ and average BJH pore diameter 11.4 nm (Figure S4 and Table 2). The diffractogram for the as-prepared inverse opal sample (Figure 7b) was characteristic for $\gamma$-$Al_2O_3$, with the broadness of the peaks suggesting that an inverse opal was composed of nanocrystalline $\gamma$-$Al_2O_3$. The data were in good accord with previous physicochemical studies of $\gamma$-$Al_2O_3$ inverse opals.[28−32] After heating at 800 °C for 4 h (Figure 7d), all peaks sharpened and intensified, consistent with an increase in the size and crystallinity of the alumina particles and a partial transformation of $\gamma$-$Al_2O_3$ to $\delta$-$Al_2O_3$.[67−76] The dominant alumina phase identified after calcinations at 1000 °C
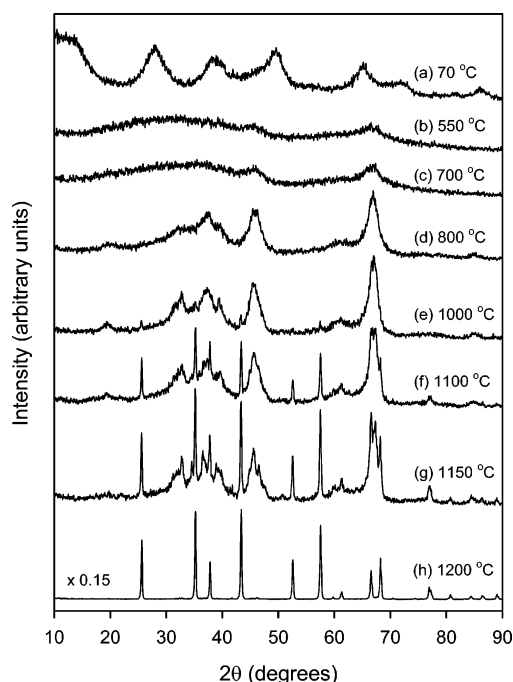
**Figure 7.** Powder XRD patterns for a $\gamma$-Al$_2$O$_3$ inverse opal powder calcined for 4 h at different temperatures up to 1200 °C. The data show the stepwise transformation of $\gamma$-Al$_2$O$_3$ → $\delta$-Al$_2$O$_3$ → $\theta$-Al$_2$O$_3$ → $\alpha$-Al$_2$O$_3$, with the formation of the latter above 1100 °C coinciding with the disappearance of the characteristic opalescence of the alumina inverse opal powder. (a) shows the XRD pattern of the $\gamma$-Al$_2$O$_3$ precursor (boehmite).



**Figure 8.** Al K-edge NEXAFS spectra for a $\gamma$-Al$_2$O$_3$ inverse opal powder calcined for 4 h at different temperatures up to 1200 °C. The data show exclusively octahedral site occupancy by Al$^{3+}$ cations for (a) the $\gamma$-Al$_2$O$_3$ precursor (boehmite) and (f) $\alpha$-Al$_2$O$_3$ obtained at 1200 °C and (b–e) combinations of tetrahedral, pentahedral, and octahedral site occupancy by Al$^{3+}$ for the transitional aluminas obtained at temperatures between 550 and 1100 °C.

**Table 2. Summarized Structural, Surface Area, and Porosity Data for $\gamma$-Al$_2$O$_3$ #1 Inverse Opal Powder Calcined at Different Temperatures up to 1200 °C; Data for a Sol−Gel Alumina Nanopowder Is Also Provided for Comparison**

| sample | calcination temp (°C) | main phase(s) by XRD | BET surface area (m² g⁻¹) | BJH pore vol (cm³ g⁻¹) | BJH mean pore diam (nm) |
|---|---|---|---|---|---|
| $\gamma$-Al$_2$O$_3$ #1 | 70[a] | Al[O]OH | 329.8 | 0.312 | 4.6 |
| | 550 | $\gamma$-Al$_2$O$_3$ | 275.5 | 0.878 | 11.4 |
| | 800 | $\gamma$-Al$_2$O$_3$, $\delta$-Al$_2$O$_3$ | 178.5 | 0.683 | 13.8 |
| | 1000 | $\theta$-Al$_2$O$_3$ | 116.7 | 0.592 | 17.9 |
| | 1100 | $\theta$-Al$_2$O$_3$, $\alpha$-Al$_2$O$_3$ | 101.3 | 0.493 | 20.5 |
| | 1200 | $\alpha$-Al$_2$O$_3$ | 13.0 | 0.078 | 25.9 |
| sol−gel $\gamma$-Al$_2$O$_3$ | 70 | Al[O]OH | 253.8 | 0.411 | 7.1 |
| | 550 | $\gamma$-Al$_2$O$_3$ | 258.1 | 0.576 | 7.8 |
| | 800 | $\gamma$-Al$_2$O$_3$, $\delta$-Al$_2$O$_3$ | 150.8 | 0.489 | 11.8 |
| | 1000 | $\theta$-Al$_2$O$_3$, $\alpha$-Al$_2$O$_3$ | 96.8 | 0.370 | 13.9 |
| | 1100 | $\theta$-Al$_2$O$_3$, $\alpha$-Al$_2$O$_3$, | 63.7 | 0.241 | 15.3 |
| | 1200 | $\alpha$-Al$_2$O$_3$ | 6.2 | 0.030 | 18.6 |

[a]Powder obtained by the hydrolysis of alminium tri-*sec*-butoxide in 2-butanol.

was $\theta$-Al$_2$O$_3$ (Figure 7e). It should be pointed out that $\gamma$-Al$_2$O$_3$, $\delta$-Al$_2$O$_3$, and $\theta$-Al$_2$O$_3$ are quite difficult to distinguish unambiguously by XRD for sol−gel derived aluminas where line broadening caused by small crystallite size complicates phase identification. Hence, quantification of the relative
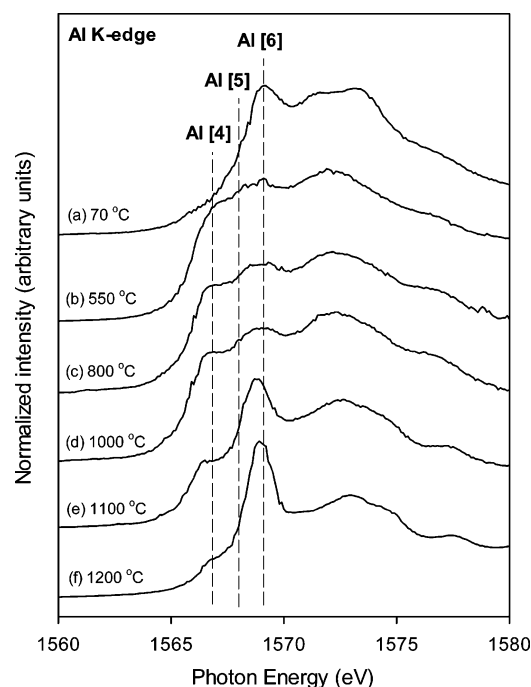
proportions of each phase at particular temperatures was not possible. The $\theta$-Al$_2$O$_3$ slowly converted to highly crystalline $\alpha$-Al$_2$O$_3$ at higher temperatures,[67−76] resulting in dramatic loss of surface area and mesoporosity (Table 2). The characteristic opalescence of the Al$_2$O$_3$ inverse opal powders was lost with calcination at 1100 °C due to crystallite growth and partial collapse of the macropores which destroyed the 3-dimensionally ordered macroporosity responsible for the opalescence. By comparison with data collected for a sol−gel $\gamma$-Al$_2$O$_3$ nanopowder (Figure S5 and Table 2), it is evident that the high-temperature phase transitions were retarded somewhat for the $\gamma$-Al$_2$O$_3$ inverse opal-derived aluminas (cf. 1100 °C), where the $\alpha$-Al$_2$O$_3$ content was ~9% for the alumina derived from the $\gamma$-Al$_2$O$_3$ inverse opal (Figure 7f) and nearly 20% for that obtained by calcining the sol−gel $\gamma$-Al$_2$O$_3$ nanopowder (Figure S5a). The macropores that exist in the Al$_2$O$_3$ inverse opal samples at such temperatures may serve to limit crystallite growth, thereby retarding the onset of the phase transitions. A similar effect has been seen by other group for non-inverse opal mesoporous $\gamma$-Al$_2$O$_3$ materials.[75,76] The fact that the inverse opal sample still retained quite high surface area (101.3 m² g⁻¹) after calcination at 1100 °C for 4 h suggests such materials could be useful in high-temperature applications involving alumina.

Al K-edge NEXAFS is a powerful tool for probing the local coordination of aluminum in aluminum-containing materials and has previously been applied to study both transitional aluminas and a variety of aluminum-containing minerals (e.g., aluminosilicates).[77−81] Absorption features at the Al K-edge give direct information about Al$^{3+}$ coordination geometry and relative site occupancy, whereas the features well above the
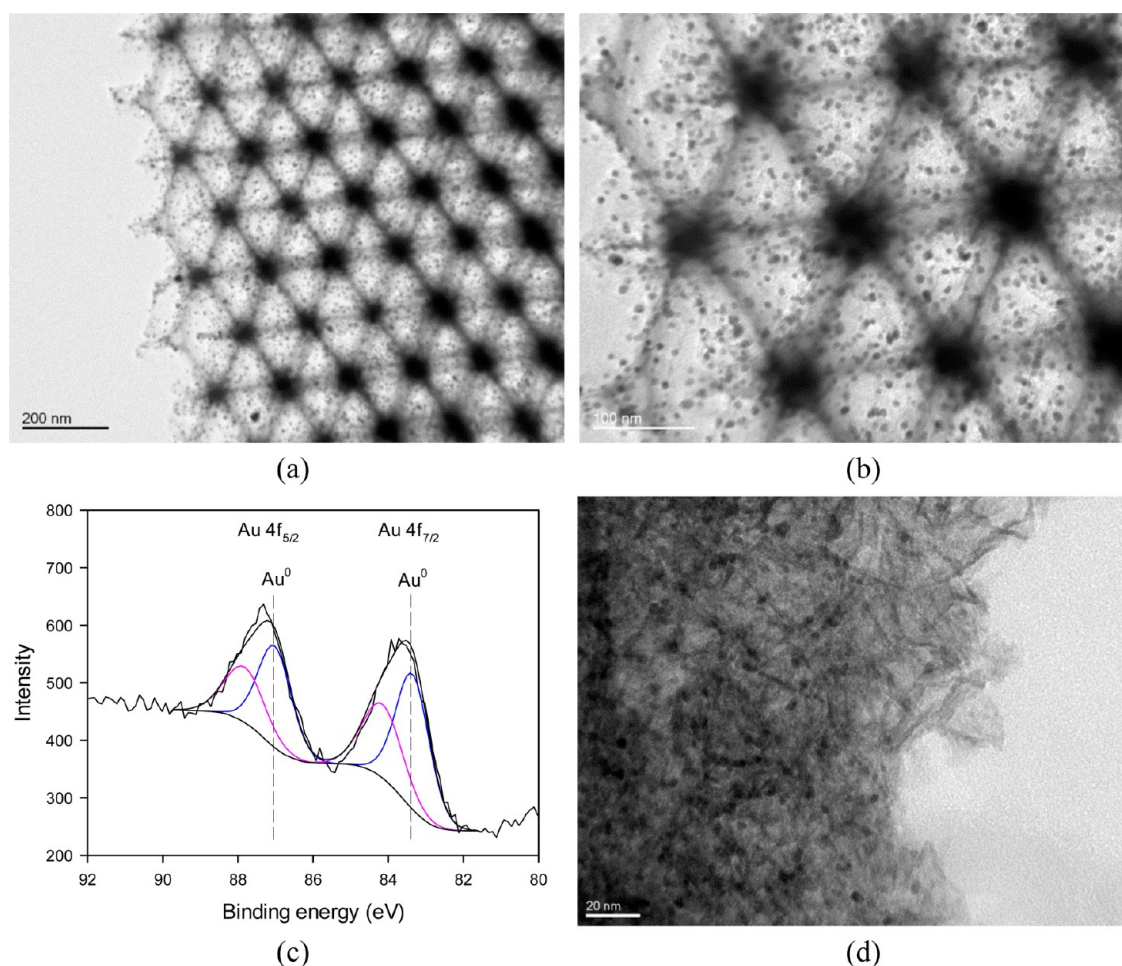
**Figure 9.** (a, b) TEM images for a 5 wt % Au/$\gamma$-Al$_2$O$_3$ inverse opal catalyst, prepared using a $\gamma$-Al$_2$O$_3$ #1 powder as the support. The images reveal well-dispersed Au nanoparticles of 5 nm mean size on the ordered macroporous support. (c) Au 4f XPS spectrum for the 5 wt % Au/$\gamma$-Al$_2$O$_3$ inverse opal catalyst, indicating the presence of Au$^0$ and an Au$^+$ species in a 2:1 ratio. (d) TEM image for the reference 5 wt % Au/$\gamma$-Al$_2$O$_3$ catalyst, prepared using a sol−gel $\gamma$-Al$_2$O$_3$ nanopowder as the support.
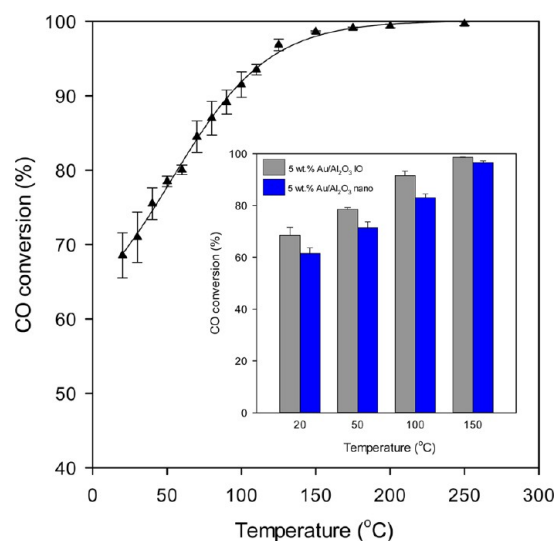


**Figure 10.** Plot of CO conversion as a function of temperature for the 5 wt % Au/$\gamma$-Al$_2$O$_3$ inverse opal catalyst, prepared using a $\gamma$-Al$_2$O$_3$ #1 powder as the support. The inset compares the activity of the 5 wt % Au/$\gamma$-Al$_2$O$_3$ catalysts prepared using the inverse opal and noninverse opal $\gamma$-Al$_2$O$_3$ supports. The catalyst with the inverse opal support demonstrated superior activity at all temperatures.

edge (at high photon energies) are due to next-nearest-neighbor effects and hence give longer range order information. The Al K-edge spectrum for the $\gamma$-Al$_2$O$_3$ IO precursor (boehmite) showed a single peak at 1569 eV (Figure 8a), characteristic of octahedrally coordinated Al$^{3+}$. The $\gamma$-Al$_2$O$_3$ inverse opal showed peaks at 1567, 1568, and 1569 eV (Figure 8b), indicating the presence of Al$^{3+}$ in tetrahedral, pentahedral, and octahedral sites. Pentahedral Al$^{3+}$ species are commonly observed for $\gamma$-Al$_2$O$_3$ nanopowders prepared by sol−gel routes[70−72] and are located exclusively as the surface of $\gamma$-Al$_2$O$_3$ nanoparticles. The theoretical tetrahedral:octahedral Al$^{3+}$ ratio for $\gamma$-Al$_2$O$_3$ is ~2:1. Attempting to determine an exact tetrahedral:octahedral ratio from Figure 8b is not practical here because of uncertainty around the position of the absorption edge which is buried under the spectrum and critical for setting up peak fitting routines. The pentahedral component disappeared following calcination at 800 °C for 4 h (Figure 8c), while a progressive increase in the tetrahedral:octahedral Al$^{3+}$ ratio was observed with calcination temperature in the range 500−1000 °C. $\theta$-Al$_2$O$_3$ (theoretical tetrahedral:octahedral ratio of 1:1) was the main alumina phase identified by XRD following calcination at 1000 °C (Figure 7e), and the corresponding Al K-edge NEXAFS spectrum (Figure 8d) was consistent with such a cation distribution. Calcination at 1200 °C resulted in the complete transformation of the sample to $\alpha$-

Al$_2$O$_3$ (exclusively octahedrally coordinated Al$^{3+}$) and near-complete disappearance of the feature at 1567 eV due to tetrahedrally coordinated Al$^{3+}$ (Figure 8f). The small residual feature at 1567 eV could potentially (but erroneously) be assigned to a tetrahedral Al$^{3+}$ species. However, recent studies have shown that this pre-edge feature seen for α-Al$_2$O$_3$ arises from atomic vibrations and electronic transitions involving the 3s empty states of the absorbing aluminum atom.[7,9−81] The EXAFS fine structure seen in the spectrum for the α-Al$_2$O$_3$ product above 1570 eV confirms the development of long-range crystalline order.

**3.4. Catalytic Activity of Au/γ-Al$_2$O$_3$ Catalysts for CO Oxidation.** Figure 9a,b shows TEM images for the 5 wt % Au/γ-Al$_2$O$_3$ IO powder, viewed along the [111] direction in the inverse opal. The TEM images confirm the successful deposition of Au nanoparticles with the preservation of the 3-dimensionally ordered macroporous structure of the support. The average Au nanoparticle size was approximately 5 nm, with the Au nanoparticle dispersed very uniformly over the support. Figure 9c shows the Au 4f XPS spectrum for the 5 wt % Au/γ-Al$_2$O$_3$ IO powder, which can be deconvoluted in to contributions from Au$^0$ (Au 4f$_{7/2}$ = 83.4 eV, Au 4f$_{5/2}$ = 87.1 eV) and a Au$^+$ species (Au 4f$_{7/2}$ = 84.2 eV, Au 4f$_{5/2}$ = 87.9 eV). The approximate ratio of the Au$^0$:Au$^+$ signals is 3:2. This was important, since previous studies of CO oxidation over Au/γ-Al$_2$O$_3$ catalysts have identified the active site as consisting of an ensemble of metallic Au atoms and a cationic Au with a hydroxyl group.[55−60] Figure 9d shows a TEM image for the reference 5 wt % Au/γ-Al$_2$O$_3$ catalyst, prepared using a sol−gel γ-Al$_2$O$_3$ nanopowder. The mean Au nanoparticle size for the reference 5 wt % Au/γ-Al$_2$O$_3$ catalyst was 6 nm. The 5 wt % Au/γ-Al$_2$O$_3$ IO catalyst and the 5 wt % Au/γ-Al$_2$O$_3$ nanopowder catalyst had near identical specific surface areas (∼210 m$^2$ g$^{-1}$), in each case slightly lower than area of the bare support.

CO oxidation data for the Au/γ-Al$_2$O$_3$ catalysts is presented in Figure 10. The 5 wt % Au/γ-Al$_2$O$_3$ IO catalyst exhibits excellent activity and stability for CO oxidation over the entire temperature range of the study, affording 69% CO conversion at 20 °C and near-complete CO conversion at 150 °C. The performance of the 5 wt % Au/γ-Al$_2$O$_3$ IO catalyst was superior to that of the 5 wt % Au/γ-Al$_2$O$_3$ nanopowder catalyst at all reaction temperatures. This difference in activity can be attributed to the ordered macroporous structure of the inverse opal support, since the physicochemical properties of the two catalysts were near identical in all other respects. It is postulated that the interconnected macropores in the inverse opal facilitate facile transport of CO and O$_2$ to the active sites, thereby increasing the global reaction rate. The results of this study parallel other recently reported studies in which catalysts based on inverse opal oxide supports were found to exhibit superior performance to catalysts synthesized using more conventional, non-inverse opal nanocrystalline oxide supports.[62,63]

## 4. CONCLUSION

γ-Al$_2$O$_3$ inverse opal thin films and powders were successfully fabricated by the colloidal crystal template technique. The photonic bandgap position for Bragg diffraction on fcc(111) planes of Al$_2$O$_3$ inverse opal thin films is dependent on the macropore diameter (which influences the interlayer spacing in [111] direction), the incident of angle of light with respect surface normal of the (111) plane, and the refractive index of the medium filling the macropores. A strong linear dependence

was established between the PBG position and solvent refractive index, demonstrating the capabilities of Al$_2$O$_3$ inverse opal thin films in optical sensing applications. γ-Al$_2$O$_3$ inverse opals possess a high specific surface area (240−275 m$^2$ g$^{-1}$) and significantly improved resistance to sintering and high-temperature phase transformations compared to conventional sol−gel γ-Al$_2$O$_3$ nanopowders. A 5 wt % Au/γ-Al$_2$O$_3$ inverse opal catalyst exhibited excellent activity for carbon monoxide oxidation at room temperature (69% conversion of CO), which can in part be attributed to the large open macropores in the inverse opal structure which allow facile diffusion of reactants to active sites (ensembles of hydroxyl groups, Au$^+$ and Au$^0$ clusters). Results of this uniquely comprehensive study of γ-Al$_2$O$_3$ inverse opal thin films and powders hint at their future potential in a diverse range of applications.

## ■ ASSOCIATED CONTENT

**ⓈSupporting Information**

Additional SEM and optical data for PMMA colloidal crystals and γ-Al$_2$O$_3$ inverse opals; N$_2$ physisorption data for a γ-Al$_2$O$_3$ inverse opal; powder XRD patterns for a reference γ-Al$_2$O$_3$ nanopowder calcined at different temperatures. This material is available free of charge via the Internet at http://pubs.acs.org.

## ■ AUTHOR INFORMATION

**Corresponding Author**

*E-mail g.waterhouse@auckland.ac.nz; Tel 64-9-9237212; Fax 64-9-373 7422 (G.I.N.W.).

**Notes**

The authors declare no competing financial interest.

## ■ ACKNOWLEDGMENTS

## ■ REFERENCES

(1) Joannopoulos, J. D.; Johnson, S. G.; Winn, J. N.; Meade, R. D. *Photonic Crystals Molding the Flow of Light*, 2nd ed.; Princeton University Press: Princeton, NJ, 2008.

(2) Joannopoulos, J. D.; Villeneuve, P. R.; Fan, S. Photonic Crystals: Putting a New Twist on Light. *Nature* **1997**, *386*, 143−149.

(3) Yablonovitch, E. Inhibited Spontaneous Emission in Solid-State Physics and Electronics. *Phys. Rev. Lett.* **1987**, *58*, 2059−2062.

(4) Takahashi, S.; Suzuki, K.; Okano, M.; Imada, M.; Nakamori, T.; Ota, Y.; Ishizaki, K.; Noda, S. Direct Creation of Three-Dimensional Photonic Crystals by a Top-Down Approach. *Nat. Mater.* **2009**, *8*, 721−725.

(5) Pang, Y. K.; Lee, J. C. W.; Lee, H. F.; Tam, W. Y.; Chan, C. T.; Sheng, P. Chiral Microstructures (Spirals) Fabrication by Holographic Lithography. *Opt. Express* **2005**, *13*, 7615−7620.

(6) Romanato, F.; Businaro, L.; Vaccari, L.; Cabrini, S.; Candeloro, P.; De Vittorio, M.; Passaseo, A.; Todaro, M. T.; Cingolani, R.; Cattaruzza.; et al. Fabrication of 3D Metallic Photonic Crystals by X-ray Lithography. *Microelectron. Eng.* **2003**, *67−68*, 479−486.

(7) Braun, P. V.; Rinne, S. A.; García-Santamaría, F. Introducing Defects in 3D Photonic Crystals: State of the Art. *Adv. Mater.* **2006**, *18*, 2665−2678.

(8) Cheng, C. C.; Arbet-Engels, V.; Scherer, A.; Yablonovitch, E. Nanofabricated Three Dimensional Photonic Crystals Operating at Optical Wavelengths. *Phys. Scr.* **1996**, *T68*, 17−20.

(9) Lin, S. Y.; Fleming, J. G.; Hetherington, D. L.; Smith, B. K.; Biswas, R.; Ho, K. M.; Sigalas, M. M.; Zubrzycki, W.; Kurtz, S. R.; Bur, J. A Three-Dimensional Photonic Crystal Operating at Infrared Wavelengths. *Nature* **1998**, *394*, 251−253.

(10) Aoki, K.; Miyazaki, H. T.; Hirayama, H.; Inoshita, K.; Baba, T.; Sakoda, K.; Shinya, N.; Aoyagi, Y. Microassembly of Semiconductor Three Dimensional Photonic Crystals. *Nat. Mater.* **2003**, *2*, 117−121.

(11) López, C. Three-Dimensional Photonic Bandgap Materials: Semiconductors for Light. *J. Opt. A: Pure Appl. Opt.* **2006**, *8*, R1−R14.

(12) von Freymann, G.; Kitaev, V.; Lotsch, B. V.; Ozin, G. A. Bottom-Up Assembly of Photonic Crystals. *Chem. Soc. Rev.* **2013**, *42*, 2528−2554.

(13) Velev, O. D.; Kaler, E. W. Structured Porous Materials via Colloidal Crystal Templating: From Inorganic Oxides to Metals. *Adv. Mater.* **2000**, *12*, 531−534.

(14) Jiang, P.; Cizeron, J.; Bertone, J. F.; Colvin, V. L. Preparation of Macroporous Metal Films from Colloidal Crystals. *J. Am. Chem. Soc.* **1999**, *121*, 7957−7958.

(15) Stein, A.; Wilson, B. E.; Rudisill. Design and Functionality of Colloidal-Crystal-Templated Materials − Chemical Applications of Inverse Opals. *Chem. Soc. Rev.* **2013**, *42*, 2763−2803.

(16) Egen, M.; Zentel, R. Large-Scale Synthesis of a Silicon Photonic Crystal with Complete Three-Dimensional Bandgap near 1.5 Micrometres. *Nature* **2000**, *405*, 437−440.

(17) Liu, X.; Zhang, Y.; Ge, D.; Zhao, J.; Li, Y.; Endres, F. Three-Dimensionally Ordered Macroporous Silicon Films Made by Electrodeposition from an Ionic Liquid. *Phys. Chem. Chem. Phys.* **2012**, *14*, 5100−5105.

(18) Suezaki, T.; O'Brien, P. G.; Chen, J. I. L.; Loso, E.; Kherani, N. P.; Ozin, G. A. Tailoring the Electrical Properties of Inverse Silicon Opals - A Step Towards Optically Amplified Silicon Solar Cells. *Adv. Mater.* **2008**, *20*, 1−5.

(19) Míguez, H.; Chomski, E.; García-Santamaría, F.; Ibisate, M.; John, S.; López, C.; Meseguer, F.; Mondia, J. P.; Ozin, G. A.; Toader, O.; et al. H.M. Photonic Bandgap Engineering in Germanium Inverse Opals by Chemical Vapor Deposition. *Adv. Mater.* **2001**, *13*, 1634−1637.

(20) Pérez, N.; Hüls, A.; Puente, D.; González-Viñas, W.; Castaño, E.; Olaizola, S. M. Fabrication and Characterization of Silver Inverse Opals. *Sens. Actuators, B* **2007**, *126*, 86−90.

(21) Schroden, R. C.; Al-Daous, M.; Blanford, C. F.; Stein, A. Optical Properties of Inverse Opal Photonic Crystals. *Chem. Mater.* **2002**, *14*, 3305−3315.

(22) Waterhouse, G. I. N.; Waterland, M. R. Opal and Inverse Opal Photonic Crystals: Fabrication and Characterization. *Polyhedron* **2007**, *26*, 356−368.

(23) Waterhouse, G. I. N.; Metson, J. B.; Idriss, H.; Sun-Waterhouse, D. Physical and Optical Properties of Inverse Opal $CeO_2$ Photonic Crystals. *Chem. Mater.* **2008**, *20*, 1183−1190.

(24) Liu, L.; Karuturi, S. K.; Su, L. T.; Tok, A. I. Y. $TiO_2$ Inverse-Opal Electrode Fabricated by Atomic Layer Deposition for Dye-Sensitized Solar Cell Applications. *Energy Environ. Sci.* **2011**, *4*, 209−215.

(25) King, J. S.; Graugnard, E.; Summers, C. J. $TiO_2$ Inverse Opals Fabricated Using Low-Temperature Atomic Layer Deposition. *Adv. Mater.* **2005**, *17*, 1010−1013.

(26) Yan, H.; Yang, Y.; Fu, Z.; Yang, B.; Xia, L.; Fu, S.; Li, F. Fabrication of 2D and 3D Ordered Porous ZnO Films Using 3D Opal Templates by Electrodeposition. *Electrochem. Commun.* **2005**, *7*, 1117−1121.

(27) Sokolov, S.; Bell, D.; Stein, A. Preparation and Characterization of Macroporous α-Alumina. *J. Am. Chem. Soc.* **2003**, *86*, 1481−1486.

(28) Li, H.; Zhang, L.; Dai, H.; He, H. Facile Synthesis and Unique Physicochemical Properties of Three-Dimensionally Ordered Macroporous Magnesium Oxide, Gamma-Alumina, and Ceria-Zirconia Solid Solutions with Crystalline Mesoporous Walls. *Inorg. Chem.* **2009**, *48*, 4421−4434.

(29) Holland, B. T.; Blanford, C. F.; Stein, A. Synthesis of Macroporous Minerals with Highly Ordered Three-Dimensional Arrays of Spheroidal Voids. *Science* **1998**, *281*, 538−540.

(30) Graugnard, E.; King, J. S.; Gaillot, D. P.; Summers, C. J. Sacrificial-Layer Atomic Layer Deposition for Fabrication of Non-Close-Packed Inverse-Opal Photonic Crystals. *Adv. Funct. Mater.* **2006**, *16*, 1187−1196.

(31) Wu, Q.-Z.; Yin, Q.; Liao, J.-F.; Deng, J.-H.; Li, Y.-G. Nitrate Route for Fabrication of Three-Dimensionally Ordered Macroporous Metal Oxides. *Acta Chim. Sin.* **2005**, *63*, 891−896.

(32) Wu, Q.-Z.; Shen, Y.; Li, Y.-G. A New Route to Fabricate Highly Ordered Three-Dimensional Macroporous $Al_2O_3$. *Acta Phys. Chim. Sin.* **2003**, *19*, 737−741.

(33) Vu, A.; Li, X.; Phillips, J.; Han, A.; Smyrl, W. H.; Bühlmann, P.; Stein, A. Three-Dimensionally Ordered Mesoporous (3DOM) Carbon Materials as Electrodes for Electrochemical Double-Layer Capacitors with Ionic Liquid Electrolytes. *Chem. Mater.* **2013**, *25*, 4137−4148.

(34) Deng, Y.; Liu, C.; Yu, T.; Liu, F.; Zhang, F.; Wan, Y.; Zhang, L.; Wang, C.; Tu, B.; Webley, P. A.; et al. Facile Synthesis of Hierarchically Porous Carbons from Dual Colloidal Crystal/Block Copolymer Template Approach. *Chem. Mater.* **2007**, *19*, 3271−3277.

(35) Zhao, L.; Tong, L.; Li, C.; Gu, Z.; Shi, G. Polypyrrole Actuators with Inverse Opal Structures. *J. Mater. Chem.* **2009**, *19*, 1653−1658.

(36) Sharma, M.; Waterhouse, G. I. N.; Loader, S. W. C.; Garg, S.; Svirskis, D. High Surface Area Polypyrrole Scaffolds for Tunable Drug Delivery. *Int. J. Pharm.* **2013**, *443*, 163−168.

(37) Kim, S.; Mitropoulos, A. N.; Spitzberg, J. D.; Tao, H.; Kaplan, D. L.; Omenetto, F. G. Silk Inverse Opals. *Nat. Photonics* **2012**, *6*, 818−823.

(38) Hong, W.; Chen, Y.; Feng, X.; Yan, Y.; Hu, X.; Zhao, B.; Zhang, F.; Zhang, F.; Xu, Z.; Lai, Y. Full-Color $CO_2$ Gas Sensing by an Inverse Opal Photonic Hydrogel. *Chem. Commun.* **2013**, *49*, 8229−8231.

(39) Hattona, B.; Mishchenko, L.; Davis, S.; Sandhage, K. H.; Aizenberg, J. Assembly of Large-Area, Highly Ordered, Crack-Free Inverse Opal Films. *Proc. Natl. Acad. Sci. U. S. A.* **2010**, *107*, 10354−10359.

(40) Cai, Z.; Liu, Y. J.; Teng, J.; Lu, X. Fabrication of Large Domain Crack-Free Colloidal Crystal Heterostructures with Superposition Bandgaps Using Hydrophobic Polystyrene Spheres. *ACS Appl. Mater. Interfaces* **2012**, *4*, 5562−5569.

(41) Stöber, W.; Fink, A.; Bohn, E. Controlled Growth of Monodisperse Silica Spheres in the Micron Size Range. *J. Colloid Interface Sci.* **1968**, *26*, 62−69.

(42) Bogush, G. H.; Tracy, M. A.; Zukoski, C. F. Preparation of Monodisperse Silica Particles: Control of Size and Mass Fraction. *J. Non-Cryst. Solids* **1988**, *104*, 95−106.

(43) Razo, D. A. S.; Pallavidino, L.; Garrone, E.; Geobaldo, F.; Descrovi, E.; Chiodoni, A.; Giorgis, F. A Version of Stöber Synthesis Enabling the Facile Prediction of Silica Nanospheres Size for the Fabrication of Opal Photonic Crystals. *J. Nanopart. Res.* **2008**, *10*, 1225−1229.

(44) Surfactant-Free Emulsion Polymerization of Various Methacrylates: Towards Monodisperse Colloids for Polymer Opals. *Macromol. Chem. Phys.* **2004**, *205*, 1479−1488.

(45) Zhang, J.; Sun, Z.; Yang, B. Self-Assembly of Photonic Crystals from Polymer Colloids. *Curr. Opin. Colloid Interface Sci.* **2009**, *14*, 103−114.

(46) Gu, Z.-Z.; Chen, H.; Zhang, S.; Sun, L.; Xie, Z.; Ge, Y. Rapid Synthesis of Monodisperse Polymer Spheres for Self-Assembled Photonic Crystals. *Colloids Surf., A* **2007**, *302*, 312−319.

(47) Wang, J.; Wen, Y.; Ge, H.; Sun, Z.; Zheng, Y.; Song, Y.; Jiang, L. Simple Fabrication of Full Color Colloidal Crystal Films with Tough Mechanical Strength. *Macromol. Chem. Phys.* **2006**, *207*, 596−604.

(48) Cong, H.; Yu, B.; Tang, J.; Li, Z.; Liu, X. Current Status and Future Developments in Preparation and Application of Colloidal Crystals. *Chem. Soc. Rev.* **2013**, *42*, 7774−7800.

(49) Biswas, R.; Sigalas, M. M.; Subramania, G.; Ho, K.-M. Photonic Band Gaps in Colloidal Systems. *Phys. Rev. B* **1998**, *57*, 3701−3705.

(50) Biswas, R.; Sigalas, M. M.; Subramania, G.; Soukoulis, C. M.; Ho, K.-M. Photonic Band Gaps of Porous Solids. *Phys. Rev. B* **2000**, *61*, 4549−4553.

(51) Busch, K.; John, S. Photonic Band Gap Formation in Certain Self-Organizing Systems. *Phys. Rev. E* **1998**, *58*, 3896−3908.

(52) Yablonovitch, E.; Gmitter, T. J. Photonic Band Structure: The Face-Centered-Cubic Case. *Phys. Rev. Lett.* **1989**, *63*, 1950−1953.

(53) Trueba, M.; Trasatti, S. P. γ-Alumina as a Support for Catalysts: A Review of Fundamental Aspects. *Eur. J. Inorg. Chem.* **2005**, 3393−3403.

(54) Fatsikostas, A. N.; Verykios, X. E. Reaction Network of Steam Reforming of Ethanol over Ni-Based Catalysts. *J. Catal.* **2004**, *225*, 439−452.

(55) Grisel, R.; Weststrate, K.-J.; Gluhoi, A.; Nieuwenhuys, B. E. Catalysis by Gold Nanoparticles. *Gold Bull.* **2002**, *35*, 39−45.

(56) Zou, X.-H.; Qi, S.-X.; Suo, Z.-H.; An, L.-D.; Li, F. Activity and Deactivation of Au/Al$_2$O$_3$ Catalyst for Low-Temperature CO Oxidation. *Catal. Commun.* **2007**, *8*, 784−788.

(57) Yan, W. F.; Ma, Z.; Mahurin, S. M.; Jiao, J.; Hagaman, E. W.; Overbury, S. H.; Dai, S. Novel Au/TiO$_2$/Al$_2$O$_3$.xH$_2$O Catalysts for CO Oxidation. *Catal. Lett.* **2008**, *121*, 209−218.

(58) Venkov, T.; Klimev, H.; Centeno, M. A.; Odriozola, J. A.; Hadjiivanov, K. State of Gold on an Au/Al$_2$O$_3$ Catalyst Subjected to Different Pre-Treatments: An FTIR Study. *Catal. Commun.* **2006**, *7*, 308−313.

(59) Quinet, E.; Morfin, F.; Diehl, F.; Avenier, P.; Caps, V.; Rousset, J.-L. Hydrogen Effect on the Preferential Oxidation of Carbon Monoxide over Alumina-Supported Gold Nanoparticles. *Appl. Catal. B: Environ.* **2008**, *80*, 195−201.

(60) Costello, C. K.; Kung, M. C.; Oha, H.-S.; Wang, Y.; Kung, H. H. Nature of the Active Site for CO Oxidation on Highly Active Au/γ-Al$_2$O$_3$. *Appl. Catal., A* **2002**, *232*, 159−168.

(61) Shimizu, K.-I.; Sugino, K.; Sawabe, K.; Satsuma, A. Oxidant-Free Dehydrogenation of Alcohols Heterogeneously Catalyzed by Cooperation of Silver Clusters and Acid−Base Sites on Alumina. *Chem.—Eur. J.* **2009**, *15*, 2341−2351.

(62) Guan, G.; Kusakabe, K.; Taneda, M.; Uehara, M.; Maeda, H. Catalytic Combustion of Methane over Pd-Based Catalyst Supported on a Macroporous Alumina Layer in a Microchannel Reactor. *Chem. Eng. J.* **2008**, *144*, 270−276.

(63) Guan, G.; Zapf, R.; Kolb, G.; Ye, J.; Zentel, R. Preferential CO oxidation over Catalysts with Well-Defined Inverse Opal Structure in Microchannels. *Int. J. Hydrogen Energy* **2008**, *33*, 797−801.

(64) Teoh, G. L.; Liew, K. Y.; Mahmood, W. A. K. Synthesis and Characterization of Sol−Gel Alumina Nanofibers. *J. Sol-Gel Sci. Technol.* **2007**, *44*, 177−186.

(65) Johnson, S. G.; Joanopoulos, J. D. Block-Iterative Frequency-Domain Methods for Maxwell's Equations in a Planewave Basis. *Opt. Express.* **2001**, *8*, 173−190.

(66) Vitanov, P.; Babeva, Tz.; Alexieva, Z.; Harizanova, A.; Nenova, Z. Optical Properties of (Al$_2$O$_3$)$_x$(TiO$_2$)$_{1-x}$ Films Deposited by the Sol-Gel Method. *Vacuum* **2004**, *76*, 219−222.

(67) Sohlberg, K.; Pennycook, S. J.; Pantelides, S. T. Hydrogen and the Structure of the Transition Aluminas. *J. Am. Chem. Soc.* **1999**, *121*, 7493−7499.

(68) Gribov, E. N.; Zavorotynska, O.; Agostini, G.; Vitillo, J. G.; Ricchiardi, G.; Spoto, G.; Zecchina, A. FTIR Spectroscopy and Thermodynamics of CO and H$_2$ Adsorbed on γ-, δ- and α-Al$_2$O$_3$. *Phys. Chem. Chem. Phys.* **2010**, *12*, 6474−6482.

(69) Ingram-Jones, V. J.; Slade, R. C. T.; Davies, T. W.; Southern, J. C.; Salvador, S. Dehydroxylation Sequences of Gibbsite and Boehmite: Study of Differences Between Soak and Flash Calcination and of Particle-Size Effects. *J. Mater. Chem.* **1996**, *6*, 73−79.

(70) Dressler, M.; Nofz, M.; Malz, F.; Pauli, J.; Jäger, C.; Reinsch, S.; Scholz, G. Aluminum Speciation and Thermal Evolution of Aluminas Resulting from Modified Yoldas Sols. *J. Solid State Chem.* **2007**, *180*, 2409−2419.

(71) Chagas, L. H.; Carvalho, G. S. G.; San Gil, R. A. S.; Chiaro, S. S. X.; Leita, A. A.; Diniz, R. Obtaining Aluminas from the Thermal Decomposition of their Different Precursors: A $^{27}$Al MAS NMR and X-ray Powder Diffraction Studies. *Mater. Res. Bull.* **2014**, *49*, 216−222.

(72) Wang, J. A.; Bokhimi, X.; Morales, A.; Novaro, O.; López, T.; Gómez, R. Aluminum Local Environment and Defects in the Crystalline Structure of Sol-Gel Alumina Catalyst. *J. Phys. Chem. B* **1999**, *103*, 299−303.

(73) Levin, I.; Brandon, D. Metastable Alumina Polymorphs: Crystal Structures and Transition Sequences. *J. Am. Ceram. Soc.* **1998**, *81*, 1995−2012.

(74) Zhou, R.-S.; Snyder, R. L. Structures and Transformation Mechanisms of the η, γ and θ Transition Aluminas. *Acta Crystallogr.* **1991**, *B47*, 617−630.

(75) Nanocrystalline Mesoporous γ-Alumina Powders "UPMC1Material" Gathers Thermal and Chemical Stability with High Surface Area. *Chem. Mater.* **2006**, *18*, 5238−5243.

(76) Yuan, Q.; Yin, A.-X.; Luo, C.; Sun, L.-D.; Zhang, Y.-W.; Duan, W.-T.; Liu, H.-C.; Yan, C.-H. Facile Synthesis for Ordered Mesoporous γ-Aluminas with High Thermal Stability. *J. Am. Chem. Soc.* **2008**, *130*, 3465−3472.

(77) Ildefonse, P.; Cabaret, D.; Sainctavit, P.; Calas, G.; Flank, A.-M.; Lagarde, P. Aluminium X-ray Absorption Near Edge Structure in Model Compounds and Earth's Surface Minerals. *Phys. Chem. Miner.* **1998**, *25*, 112−121.

(78) Kato, Y.; Shimizu, K.-I.; Matsushita, N.; Yoshida, T.; Yoshida, H.; Satsuma, A.; Hattori, T. Quantification of Aluminium Coordinations in Alumina and Silica-Alumina by Al K-Edge XANES. *Phys. Chem. Chem. Phys.* **2001**, *3*, 1925−1929.

(79) Brouder, C.; Cabaret, D.; Juhin, A.; Sainctavit, P. Effect of Vibrations on the Pre-edge Features of X-ray Absorption Spectra. *Phys. Rev. B* **2010**, *81*, 115125.

(80) Manuel, D.; Cabaret, D.; Brouder, C.; Sainctavit, P.; Bordage, A.; Trcera, N. Experimental Evidence of Thermal Fluctuations on the X-ray Absorption Near-Edge Structure at the Aluminum K Edge. *Phys. Rev. B* **2012**, *85*, 224108.

(81) Cabaret, D.; Brouder, C. Origin of the Pre-edge Structure at the Al K-edge: The Role of Atomic Vibrations. *J. Phys. Conf. Ser.* **2009**, *190*, 012003.